An investigation of the electrical dynamics in electroactive polymer transducers with resistive electrodes

Davide Vignotto[1] **, Antonello Cherubini**[1]**, Ion-Dan Sîrbu**[2] **, Marco Fontana**[2] **and Giacomo Moretti**[1,*]

[1] Department of Industrial Engineering, University of Trento, Trento, Italy
[2] Institute of Mechanical Intelligence, Scuola Superiore Sant'Anna, Pisa, Italy

E-mail: giacomo.moretti@unitn.it

CrossMark

Abstract

To pursue a variable-capacitance working principle, transducers based on soft electroactive polymers (EAPs) need deformable electrodes that match the compliance and stretchability of the EAP polymeric substrates. A variety of manufacturing procedures are available to create conductive materials that can achieve this, including solutions that can provide remarkably low resistivity. However, the simplest and most feasible options often involve the use of particle-filled (e.g. carbon-filled) polymer composites, which, while easy to produce, tend to exhibit relatively high resistivity. This high level of resistivity, combined with the inherent capacitance of EAP transducers, introduces dynamic effects in the devices electrical activation, which may affect performance. This paper investigates the impact of electrode resistivity on the electrical dynamics of EAP devices, combining continuum models and experimental validations. We use a continuum generalisation of known resistive-capacitive (RC) transmission line models to accurately predict voltage gradients on the surfaces of electrostatic transducers subject to rapidly varying voltages. We then present an experimental validation by measuring the spatial voltage distributions over carbon-based polymeric electrodes of dielectric elastomer (DE) transducers, and find a good agreement with our model predictions. We use our validated model to provide general estimates of the typical charging time and limit working frequency ranges of DE devices as a function of their dimensional scale and electrode sheet resistance. Our model provides useful indications for designing compliant electrodes in EAP transducers given target performance, or to understand the working limits of devices with given geometry and dielectric-electrode properties.

Keywords: dielectric elastomer, electrode, transmission line, electroactive, polymer, sheet resistance

---

* Author to whom any correspondence should be addressed.

1. Introduction

Electrostatic transducers based on electroactive polymers (EAPs) are a promising class of devices that generate an actuation output (force or stroke) in response to an electric field or, viceversa, leverage mechanically driven deformations and cyclic electric loading to convert input mechanical energy into electrical energy [1]. Among EAP devices, dielectric elastomer (DE) transducers, which are variable capacitors with stretchable polymeric dielectrics, have gathered significant scientific attention, owing to their high energy density and inherent compliance [2]. While, on the one hand, DEs have established themselves as a potentially promising alternative to electromagnetic drives for robotics [3], fluidics [4], acoustic applications [5] and energy harvesting [6], breakthroughs in the field of EAP drives continue to emerge, which leverage new principles or material solutions, such as recently developed liquid-gap zipping actuators [7–9] (figure 1).

One of the most critical components in EAP transducers are compliant electrodes, which are required to preserve their conductivity while complying with the deformations of the flexible dielectric substrates they are applied on [10, 11]. The limitation in conductivity due to materials' resistivity is a key factor, as it affects bandwidth (namely, the charging/discharging time constants) and energy efficiency of transducers. This is particularly relevant in applications that involve large-scale devices (such as power-scale energy harvesting based on DEs [6, 12]), or high-frequency applications (such as acoustic applications [13–16]). The former might indeed be characterised by large resistor-capacitor (RC) time constants, whereas the latter demand for fast charging/discharging times.

Whereas laboratory EAP prototypes often rely on carbon-based grease or spray electrodes [11], which are practical for rapid prototyping but vulnerable to desiccation and material migration, different principles to manufacture stable and scalable compliant electrodes have also been investigated. These include casting [17], screen [18, 19], pad [20] or inkjet printing [21–23] of polymer-based mixtures containing carbon black (CB) [17], graphite [24], carbon nanotubes [21], or metal vapour deposition [25, 26] and ion implantation [27, 28] to form nanometre-thin metal layers. Although metal electrodes can reach sheet resistances often significantly below 100 $\Omega \square^{-1}$ [11, 25, 29–31], they necessitate corrugation or complex patterned designs to accommodate their limited elasticity. Carbon-based electrodes have been extensively investigated, as they can maintain electrical conductivity under strains. Ultra-compliant carbon powders typically deposited on adhesive dielectric substrates were reported to exhibit sheet resistances R_s in the range $10 - 160$ k$\Omega \square^{-1}$ [11, 21, 24, 32–36] in their undeformed state. Electrodes based on carbon nanotubes were reported to achieve sheet resistances as low as 0.1 k$\Omega \square^{-1}$ [37], but they are prone to mechanical abrasion and carbon contamination of the environment.

To describe the effect of the electrodes' resistivity on a transducer's behaviour, in past works reference has been primarily made to lumped-parameter approaches, based on equivalent circuit representations, in which the electrodes' contribution was modelled as a lumped resistance in-series to the DE capacitance [14, 38, 39]. Though lumped-parameter approaches are effective in capturing charging/discharging dynamics of DE transducers and for the implementation of self-sensing algorithms [38, 40, 41], the RC dynamics in EAP devices are inherently continuum phenomena. Similar to RC transmission lines [42], quick charging/discharging of an EAP transducer results in voltage gradients over the device surface.

Approaches to model or exploit spatial voltage distributions owing to the electrodes' resistivity in EAPs have been explored by a few groups in the past. Anderson *et al* used transmission networks to model DE systems and develop advanced sensor concepts. [43–45]. They first used a transmission line model to describe DE actuator stacks with a large number of layers [43]. They explained voltage gradients throughout the layers using a network model with RC elements modelling the different layers, and resistive elements accounting for the interconnect resistances. They suggested that such a network structure can be used to determine upper bounds for the frequency of the probing signals used in self-sensing applications. Later, they used RC network models to describe space gradients within a same DE sample, using RC elements to describe the resistance/capacitance of different portions of the electrodes/DE material. Based on that, they developed stretch sensors that can measure local inputs through a single measurement channel, via reactance measurements at different frequencies [45].

Graf and Maas [46] resorted for the first time to continuum formulations to describe the dynamic electric field distribution over DE membranes. They cast a theoretical continuum model (in the form of a diffusion equation) for a rectangular DE membrane, found analytical solutions for the field distribution, and used them to optimise the distribution of electrode contacts to minimise spatial field gradients.

Garnell *et al* [47] proposed a fully-coupled electromechanical model of the response of DE membranes with resistive electrodes. They highlighted couplings between the vibratory response and voltage distributions due to electrode resistivity, and validated them with local velocity measurements. However, as their focus was set on the membranes' vibratory response, they did not perform local measurements of voltage distributions.

This paper presents a general continuum time-domain model and its experimental validation for the voltage distribution in capacitors with mildly resistive electrodes. We resort to an analytical diffusion model that allows calculating space and voltage distribution of charge/electric potential on the surfaces of electrodes, given a set of boundary conditions. While building upon an approach and formulation similar to that presented in [46], our formulation holds for thin-shell capacitors with generic shapes (including non-uniform thickness/electric properties), and can thus be used to describe different classes of EAP transducers that rely on thin-film dielectric gaps, and integrated with continuum electromechanical models [47]. We present a set of analytical solutions (cast as Fourier series expansions) for simple geometries
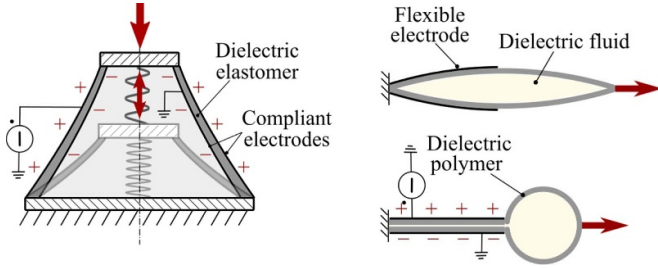
Figure 1. Examples of EAP transducers with compliant electrodes (cross-section view): DE actuator (left) and fluid-based zipping actuator (right).

(rectangular strip or circular capacitors) subject to prototypical voltage excitation waveforms (step, sine response). To validate such continuum models, we performed voltage measurements at different points on the surface of silicone-based DE transducers featuring carbon-loaded polymer-based electrodes [17]. To overcome measurement issues due to contact resistance (which can be comparable to or higher than the electrode resistance if a simple push contact is established with the measurement circuit wires [48, 49]), we embedded a number of measurement pick-up contacts directly into the compliant electrodes bulk. We show that applying high-frequency excitation on the transducer through its perimeter leads to non-uniform voltage distributions (with a decrease in amplitude far apart from the excitation surfaces), which is accurately captured by the diffusion model presented. This model constitutes a general tool to determine bandwidth limits and distributions of the applied electric field in EAP transducers based on their electrodes sheet resistance, or, conversely, to design connections among compliant electrodes and circuit wires in order to obtain desired bandwidth and charging time.

Though multi-point resistance measurements on DE samples have been done in the past (mostly in combination with carbon grease electrodes [50]), to the best of our knowledge this is the first work in which continuum electrical models are validated against local measurements on DE prototypes based on technically-relevant material combinations.

The rest of the paper is structured as follows. Section 2 presents the theoretical model formulation. Section 3 presents the experimental setup and validation. Section 4 presents a discussion on the implications of practical sheet-resistance values on the bandwidth and performance of practical EAP transducers. Finally, section 5 presents the conclusions.

2. Voltage distribution on capacitive transducers with resistive electrodes

2.1. Problem formulation

We hereby formulate a dynamic model to calculate the voltage distribution over time on a generic electrostatic transducer with resistive electrodes. As compared to previous works [46],

our model holds for generic transducer and electrode geometries (e.g. variable thickness dielectrics/electrodes, asymmetrical electrodes layout).

For the sake of illustration, we assume that the transducer consists of a single ideal dielectric shell (though the formulation can be easily generalised to the case of multi-layer dielectrics), covered by adhered electrodes on both faces, as shown in figure 2. We also assume that the transducer geometry is kept fixed so that the state variations only involve electrical variables. In the case of practical EAP transducers, this latter assumption holds true because mechanical dynamics typically are orders of magnitude slower than electrical dynamics. The dielectric layer is a thin shell, thus opposing faces are assumed to have the same curvature. The perimeters of the two electrodes hold some portions that are subject to an external voltage, and others that are let free (i.e. with no current flowing through). From an electrical viewpoint, the system is equivalent to a continuous network of capacitors and resistors (with infinitesimal capacitance/resistance), as illustrated in figure 2(right). [42, 51, 52].

We define a set of curvilinear coordinates $\boldsymbol{\xi} = [\xi_1, \xi_2]^\intercal$, which uniquely identify a point on the shell surface. We denote $v^+ = v^+(\boldsymbol{\xi}, t)$ and $v^- = v^-(\boldsymbol{\xi}, t)$ the voltage distributions on the two electrodes, which are functions of the position $\boldsymbol{\xi}$ and the time t.

We isolate an infinitesimal portion of the capacitor with infinitesimal side lengths $d\xi_1$ and $d\xi_2$, local dielectric thickness $t_d = t_d(\boldsymbol{\xi})$ and electrodes thickness $t_e = t_e(\boldsymbol{\xi})$, here assumed equal for both electrodes for simplicity.

We denote $\boldsymbol{\lambda}_i^+ = [\lambda_{i1}^+, \lambda_{i2}^+]^\intercal$ and $\boldsymbol{\lambda}_i^- = [\lambda_{i1}^-, \lambda_{i2}^-]^\intercal$ the vectors of the linear current density (namely, the current per unit length in the electrode perpendicular planar direction) on the positive and negative electrodes respectively, holding components both along ξ_1 and ξ_2. Denoting $\kappa_e = \kappa_e(\boldsymbol{\xi})$ the local conductivity of the electrodes, the voltage drop in the direction of ξ_1 on an infinitesimal portion of the top electrode reads as follows, according to Ohm's laws:

$$ dv^+ = - \underbrace{\frac{d\xi_1}{\kappa_e t_e \, d\xi_2}}_{\text{resistance}} \cdot \underbrace{\lambda_{i1}^+ \, d\xi_2}_{\text{current}}. \tag{1} $$

Noting that similar considerations hold for the voltage drop in direction ξ_2 and for both electrodes, the current linear densities can be simply expressed as follows

$$ \boldsymbol{\lambda}_i^+ = -\frac{1}{R_s} \nabla v^+ = -\frac{1}{R_s} \left[\frac{\partial v^+}{\partial \xi_1}, \frac{\partial v^+}{\partial \xi_2} \right]^\intercal, $$
$$ \boldsymbol{\lambda}_i^- = -\frac{1}{R_s} \nabla v^- = -\frac{1}{R_s} \left[\frac{\partial v^-}{\partial \xi_1}, \frac{\partial v^-}{\partial \xi_2} \right]^\intercal $$
$$ \text{with} \quad R_s = (\kappa_e t_e)^{-1} \tag{2} $$

where ∇ denotes the gradient operator in the plane directions, and R_s represents the local sheet resistance of the electrode, which generally varies along the transducer's surface
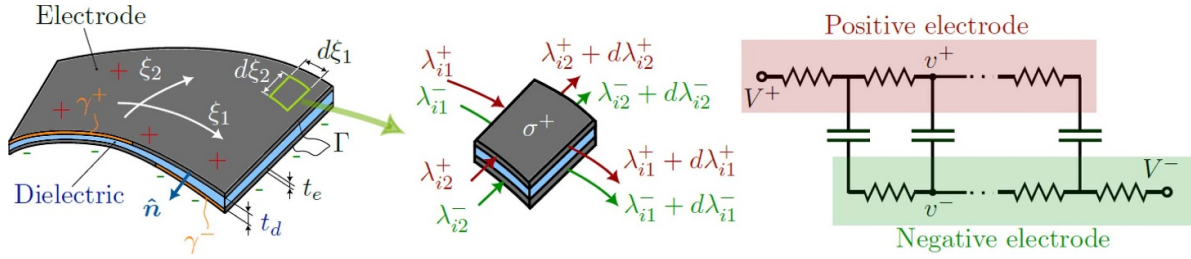
Figure 2. Model symbols definition: generic representation of an electrostatic transducer with resistive electrodes (left); charge balance on an infinitesimal element (centre); equivalent RC circuit (right).

(e.g. as a result of a non-uniform or deformed electrode thickness).

We denote $\sigma^+ = -\sigma^- = \sigma$ the local charge surface density on the positive/negative electrode portions of the infinitesimal capacitor element. With reference to the positive electrode, we cast the charge balance as follows:

$$d\xi_1 d\xi_2 \frac{\partial \sigma}{\partial t} = -d\xi_2 d\lambda_{i1}^+ - d\xi_1 d\lambda_{i2}^+ \tag{3}$$

where the first term represents the charge stored on the infinitesimal capacitor patch per unit time, and the terms on the right hand side represent the differences between the charge flow rates flowing out of the capacitor and those flowing in, in both surface directions.

Rearranging the differential terms and replacing the current densities with the expressions given by (2) leads to:

$$\frac{\partial \sigma}{\partial t} = +\frac{\partial}{\partial \xi_1}\left(\frac{1}{R_s}\frac{\partial v^+}{\partial \xi_1}\right) + \frac{\partial}{\partial \xi_2}\left(\frac{1}{R_s}\frac{\partial v^+}{\partial \xi_2}\right). \tag{4}$$

Similar considerations can be done for the negative electrode, referring to voltage distribution v^- and observing that the accumulated charge is negative, which lead to the following equation:

$$\frac{\partial \sigma}{\partial t} = -\frac{\partial}{\partial \xi_1}\left(\frac{1}{R_s}\frac{\partial v^-}{\partial \xi_1}\right) - \frac{\partial}{\partial \xi_2}\left(\frac{1}{R_s}\frac{\partial v^-}{\partial \xi_2}\right). \tag{5}$$

Defining the capacitance of an infinitesimal patch of transducer allows putting σ in relation to v^+ and v^-:

$$\underbrace{\sigma\, d\xi_1 d\xi_2}_{\text{charge}} = \underbrace{\frac{\varepsilon\, d\xi_1 d\xi_2}{t_d}}_{\text{capacitance}}\left(v^+ - v^-\right), \tag{6}$$

where ε is the dielectric medium's permittivity (for multi-material layered dielectrics, the equation still holds, provided that an equivalent series permittivity is introduced).

Replacing (6) into (4) and (5) leads to the following system of partial differential equations (PDEs):

$$\frac{\partial (v^+ - v^-)}{\partial t} = \frac{t_d}{\varepsilon}\left[\frac{\partial}{\partial \xi_1}\left(\frac{1}{R_s}\frac{\partial v^+}{\partial \xi_1}\right) + \frac{\partial}{\partial \xi_2}\left(\frac{1}{R_s}\frac{\partial v^+}{\partial \xi_2}\right)\right],$$

$$\frac{\partial (v^+ - v^-)}{\partial t} = -\frac{t_d}{\varepsilon}\left[\frac{\partial}{\partial \xi_1}\left(\frac{1}{R_s}\frac{\partial v^-}{\partial \xi_1}\right) + \frac{\partial}{\partial \xi_2}\left(\frac{1}{R_s}\frac{\partial v^-}{\partial \xi_2}\right)\right]. \tag{7}$$

Equating the right hand sides of the two equations allows recasting (7) as a system of a diffusion PDE (holding time derivatives of the voltages) and a Laplace-like PDE [53].

Adding to the equations a set of initial conditions (ICs) and boundary conditions (BCs) provides the following PDE problem, in which v^+ and v^- are the unknowns:

$$\begin{cases} \dfrac{\partial (v^+ - v^-)}{\partial t} = \dfrac{t_d}{\varepsilon}\left[\dfrac{\partial}{\partial \xi_1}\left(\dfrac{1}{R_s}\dfrac{\partial v^+}{\partial \xi_1}\right) + \dfrac{\partial}{\partial \xi_2}\left(\dfrac{1}{R_s}\dfrac{\partial v^+}{\partial \xi_2}\right)\right] \\[4mm] \dfrac{\partial}{\partial \xi_1}\left(\dfrac{1}{R_s}\dfrac{\partial (v^+ + v^-)}{\partial \xi_1}\right) + \dfrac{\partial}{\partial \xi_2}\left(\dfrac{1}{R_s}\dfrac{\partial (v^+ + v^-)}{\partial \xi_2}\right) = 0 \\[4mm] v^+\left(\boldsymbol{\xi},t\right)\big|_{\gamma^+} = V^+\left(t\right) \\[2mm] \left(\nabla v^+\left(\boldsymbol{\xi},t\right)\cdot\hat{\boldsymbol{n}}\right)\big|_{\Gamma\backslash\gamma^+} = 0 \\[2mm] v^-\left(\boldsymbol{\xi},t\right)\big|_{\gamma^-} = V^-\left(t\right) \\[2mm] \left(\nabla v^-\left(\boldsymbol{\xi},t\right)\cdot\hat{\boldsymbol{n}}\right)\big|_{\Gamma\backslash\gamma^-} = 0 \\[2mm] v^+\left(\boldsymbol{\xi},0\right) = v^-\left(\boldsymbol{\xi},0\right) = v_0\left(\boldsymbol{\xi}\right) \end{cases}. \tag{8}$$

Here, we denote Γ the electrode frontier (same for both electrodes), and γ^+ (γ^-) a portion of the positive (negative) electrodes frontier where external voltages V^+ and V^- (with $V^- < V^+$) - generally time-varying - are applied (Dirichlet BC). In the free portions of the electrodes' frontier (denoted $\Gamma \backslash \gamma^+$ and $\Gamma \backslash \gamma^-$ for the two electrodes), no current can flow perpendicularly to the edges (whose normal external unit vector is denoted $\hat{\boldsymbol{n}}$). Using relationship (2) between current and voltage gradient thus results in a Neumann-type homogeneous BC.

Assuming that the capacitor is initially uncharged ($\sigma(\boldsymbol{\xi},0) = 0$), both electrodes hold the same voltage distribution $v(\boldsymbol{\xi},0) = v_0(\boldsymbol{\xi})$ at $t=0$, based on (6). The determination of $v_0(\boldsymbol{\xi})$ requires the solution of an additional PDE problem, as detailed in the appendix.
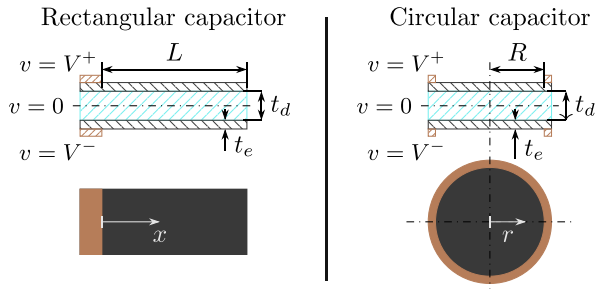
Figure 3. Rectangular strip and circular capacitor: variables definition. The copper-colour strips are the excitation contacts. Assuming symmetrical geometry and excitation ($V^- = -V^+$), the middle plane is iso-potential with zero voltage.

If the sheet resistance R_s is uniform throughout the electrodes, PDE (8) takes the following simplified form:

$$
\begin{cases}
\dfrac{\partial (v^+ - v^-)}{\partial t} = \alpha \nabla^2 v^+, \ \text{with} \ \alpha = \dfrac{t_d}{\varepsilon R_s} \\
\nabla^2 (v^+ + v^-) = 0 \\
v^+ (\boldsymbol{\xi}, t)\big|_{\gamma^+} = V^+(t) \\
\left(\nabla v^+ (\boldsymbol{\xi}, t) \cdot \hat{\boldsymbol{n}} \right)\big|_{\Gamma \setminus \gamma^+} = 0 \\
v^- (\boldsymbol{\xi}, t)\big|_{\gamma^-} = V^-(t) \\
\left(\nabla v^- (\boldsymbol{\xi}, t) \cdot \hat{\boldsymbol{n}} \right)\big|_{\Gamma \setminus \gamma^-} = 0 \\
v^+ (\boldsymbol{\xi}, 0) = v^- (\boldsymbol{\xi}, 0) = v_0 (\boldsymbol{\xi})
\end{cases}
\tag{9}
$$

where ∇^2 is the Laplace operator (with respect to $\boldsymbol{\xi}$), and coefficient α has dimensions of $m^2 \ s^{-1}$ and plays the role of a diffusion coefficient. Indeed, the first equation in (9) has the well-known form of a diffusion equation (heat equation) [53]. Note that, once a solution for v^+ and v^- is available, equation (2) allows calculating the total supplied current i (and, hence, power) upon integration over the excitation surfaces:

$$
i = -\int_{\gamma^+} \frac{1}{R_s} \nabla v^+ \cdot \hat{\boldsymbol{n}} \, dl = \int_{\gamma^-} \frac{1}{R_s} \nabla v^- \cdot \hat{\boldsymbol{n}} \, dl,
\tag{10}
$$

where the integrals are calculated over the length of surfaces γ^+ or γ^-.

In the following, we focus our attention on two simple examples for which analytical solutions to (9) can be found. Namely, referring to figure 3, the examples are a rectangular strip capacitor (with a uniform voltage applied on one edge) and a circular capacitor (with a uniform voltage applied on the perimeter). Both examples are representative of technically relevant DE topologies [54, 55].

2.2. 1D rectangular geometry

We consider a rectangular strip of dielectric material with length L covered by two identical resistive electrodes, each subject to a prescribed voltage (V^+ and V^-). This geometry represents a prototypical example of a DE transducer [56], and has been taken as a benchmark by previous works on the electrodynamic field distribution in DEs [46]. Assuming that the

excitation is uniformly applied along the whole strip width, the voltage distribution on the electrodes can be assumed uni-dimensional, therefore it only depends on a linear coordinate x and time. Moreover, assuming for simplicity that $V^+(t) = -V^-(t) = V(t)$ (removing this assumption simply introduces an offset in the voltage distribution), the voltages on the electrodes are equal and opposite: $v^+(x,t) = -v^-(x,t) = v(x,t)$, and the mid-plane of the device (parallel to the electrodes, halfway through the thickness of the dielectric) is an iso-potential symmetry plane with $v = 0$. Under the assumption of uniform sheet resistance, (9) takes the following reduced form:

$$
\begin{cases}
\dfrac{\partial v}{\partial t} = \alpha' \dfrac{\partial^2 v}{\partial x^2}, \\
v(0,t) = V^+(t) \\
\dfrac{\partial v}{\partial x}(L,t) = 0 \\
v(x,0) = 0
\end{cases}
\tag{11}
$$

with $\alpha' = \alpha/2$, for which analytical solutions can be found depending on the form of $V^+(t)$. We introduce a set of dimensionless quantities:

$$
x^* = \frac{x}{L}, \quad t^* = \frac{\alpha' t}{L^2}, \quad v^* = \frac{v}{V_0}
\tag{12}
$$

where V_0 is a constant reference voltage (e.g. the amplitude or peak value of function $V^+(t)$) and then we re-cast the PDE in (11) in a dimensionless form as follows:

$$
\begin{cases}
\dfrac{\partial v^*}{\partial t^*} = \dfrac{\partial^2 v^*}{\partial x^{*2}} \\
v^*(0,t^*) = \dfrac{V^+}{V_0} \\
\dfrac{\partial v^*}{\partial x^*}(1,t^*) = 0 \\
v^*(x^*,0) = 0
\end{cases}
\tag{13}
$$

We hereby present solutions to (13) considering some prototypical voltage excitation waveforms (step, sine), with the aim of highlighting relevant trends in terms of time- and frequency-domain response, and spatial distribution of the voltage.

2.2.1. Step response.
Applying a constant voltage V_0 on the initially uncharged capacitor ($v^*(0,t^*) = 1$) leads to the following voltage distribution (in dimensionless form):

$$
v^*(x^*,t^*) = 1 - 2 \sum_{n=0}^{+\infty} \frac{e^{-\gamma_n t^*}}{\gamma_n} \sin(\gamma_n x^*)
\tag{14}
$$

with $\gamma_n = (n + 1/2)\pi$

whose expression as a Fourier series has been obtained by solving (13) via separation of variables [53]. Figure 4(top left) shows that the voltage holds a non-uniform distribution over the electrode surface, which progressively flattens to a constant value ($v^* = 1$), as previously observed in [46]. While v^* at the excitation edge ($x^* = 0$) is constant and equal to 1, the
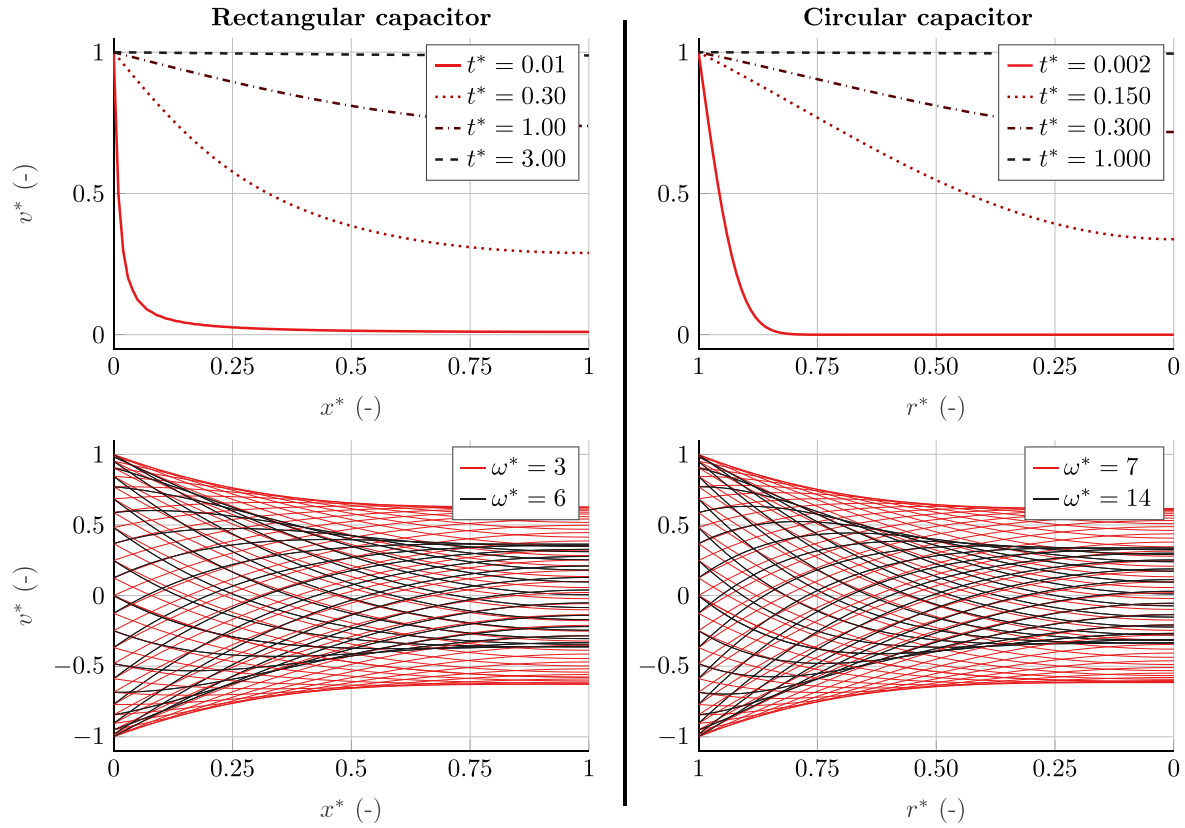
Figure 4. Dimensionless plots of the voltage distributions over rectangular (left) and circular (right) capacitors, subject to a voltage step (top) and sinusoidal excitation (bottom). All plots have been obtained truncating the series expansions to $n = 50$ harmonics. In the plots, different lines refer to different time instants (lines in the bottom plots hold a dimensionless time spacing of 0.02).

voltage at the capacitor free edge rises from 0 to 1 following a diffusion dynamics. The voltage reaches an average value equal to 99% the target value at the far free edge in a (dimensionless) time $t^* \simeq 2.8$. On a practical transducer, the physical charging time increases with the square of the length L, the sheet resistance R_s and the ratio ε/t_d (i.e. proportionally to the device capacitance), according to (12).

2.2.2. Sinusoidal response. We evaluate the steady-state response of the strip capacitor to sinusoidal voltages in the form $v^* = \sin \omega t = \sin \omega^* t^*$, where $\omega^* = \omega L^2/\alpha$ is the angular frequency associated to the dimensionless time t^* defined in (12). The resulting dimensionless voltage distribution in steady-state conditions (omitting the initial transient response) reads as follows:

$$
v^*\left(x^*, t^*\right) = \sin\left(\omega^* t^*\right) - \sum_{n=0}^{+\infty} \frac{2\omega^*}{\gamma_n} \sin\left(\gamma_n x^*\right) \cdot
$$
$$
\cdot \left(\frac{\omega^* \sin\left(\omega^* t^*\right) + \gamma_n^2 \cos\left(\omega^* t^*\right)}{\omega^{*2} + \gamma_n^4} \right)
\tag{15}
$$

where $\gamma_n = (n + 1/2)\pi$.

Figure 4(bottom left) shows the profiles of the dimensionless steady-state voltage over the strip length at different time instants spaced apart by 0.02 dimensionless time units (each

curve represents the profile at a given time), for two different excitation frequencies ($\omega^* = 3$ and 6). The envelope of the profiles shows that the oscillation amplitude of the voltage is maximum at the excited edge (where voltage is applied) and minimum at the far free edge. Gradients in the voltage amplitude are larger close to the excited edge, whereas the oscillation amplitude is roughly constant in a broad region close to the free edge. This result indicates that exciting the capacitor with high-frequency would ultimately lead to a non-uniform distribution of the voltage, with regions far from the contacts with the circuit being constantly subject to lower electric field than the nominal prescribed value. In practical systems (e.g. EAP actuators and loudspeakers), this means that the dielectric material is not exploited evenly, with peripheral regions being subject to a fraction of the nominal Maxwell stress. Using (15), we found that the amplitude of the voltage at the strip free edge is at least 99% the amplitude at the excitation node provided if $\omega^* < 0.4$, and 90% the excitation amplitude if $\omega^* < 1.2$.

2.3. Axial-symmetrical circular geometry

We consider a circular capacitor with radius R and resistive electrodes (figure (3)), uniformly excited on the outer perimeter of the two electrodes. Owing to the axial symmetry of the problem, the voltage distribution only depends on the radial coordinate r and time: $v = v(r, t)$. Similar to the previous

case, we assume that opposite electrodes are excited with opposite voltages, leading to $v^+(r,t) = -v^-(r,t) = v(r,t)$. Casting Laplace operator in polar coordinates, defining a dimensionless radial coordinate $r^* = r/R$ and using the other dimensionless parameters as in (12) leads to the following PDE:

$$
\begin{cases}
\dfrac{\partial v^*}{\partial t^*} = \dfrac{1}{r^*}\dfrac{\partial}{\partial r^*}\left(r^*\dfrac{\partial v^*}{\partial r^*}\right) \\[2mm]
\dfrac{\partial v^*}{\partial r^*}(0,t^*) = 0 \\[2mm]
v^*(1,t^*) = \dfrac{V^+}{V_0} \\[2mm]
v^*(r^*,0) = 0
\end{cases}
\tag{16}
$$

where the BC at $r^* = 0$ owes to symmetry.

2.3.1. Step response. Similar to the rectangular case, we solve (16) assuming that a voltage step, $v^*(1,t^*) = 1$, is applied on the circular capacitor's perimeter. The Fourier series expansion of the solution reads as follows:

$$
v^*(r^*,t^*) = 1 - \sum_{n=1}^{\infty} \frac{2J_0(\beta_n r^*)}{\beta_n J_1(\beta_n)} e^{-\beta_n^2 t^*},
\tag{17}
$$

where J_k denotes a Bessel function of the first kind and order k, and β_n a sequence of zeros of zero-order first-kind Bessel function J_0.

A plot of the voltage distribution on the circular electrode in response to a voltage step is shown in figure 4(top right). The trend is similar to that previously observed for a strip capacitor, with the dimensionless voltage at the capacitor's centre progressively rising from 0 to 1. The mean value of the voltage reaches 99% of the set-point value in a dimensionless time of 0.8, i.e. lower than that of a rectangular capacitor. In practice, this means that a circular capacitor with radius equal to the length of a rectangular strip capacitor featuring same dielectric and electrode properties would fully charge in a shorter time. This entirely owes to geometrical factors, i.e. the fact that in an axial-symmetrical capacitor current is uniformly supplied through the entire device perimeter and flows through concentric electrode surfaces.

2.3.2. Sinusoidal response. Applying a sinusoidal voltage excitation (as in section 2.2.2) leads to a steady-state response in the following form:

$$
\begin{aligned}
v^*(r^*,t^*) = {}& \sin(\omega^* t^*) - 2\sum_{n=1}^{+\infty} \frac{1}{\beta_n} \frac{J_0(\beta_n r^*)}{J_1(\beta_n)} \\
& \cdot \omega^*\left(\frac{\omega^*\sin(\omega^* t^*) + \beta_n^2\cos(\omega^* t^*)}{\omega^{*2} + \beta_n^4}\right).
\end{aligned}
\tag{18}
$$

The corresponding dimensionless plots, showing the voltage profiles on a circular electrode at different time instants for two different excitation frequencies ($\omega^* = 7$ and 14), are shown in figure 4(bottom right). These profiles are qualitatively similar to those obtained for a rectangular capacitor,

with the quantitative difference that frequencies required to induce radial amplitude gradients comparable to axial gradients obtained in the previous case are larger. The voltage amplitude at the capacitor centre is at least 99% the excitation voltage amplitude if $\omega^* < 0.8$ and 90% if $\omega^* < 2.8$ (as opposed to 0.4 and 1.2 of strip capacitors) denoting a broader bandwidth that a counterpart rectangular capacitor with length equal to the radius and same dielectric/electrode layers composition.

3. Experimental validation

We validated the model presented in section 2.1 on practical electrostatic transducer systems, consisting of a widely used DE material with carbon-loaded polymer based electrodes. We carried out a validation by performing measurements of voltage distributions over multiple points on the electrodes of transducers with different geometries, subjected to sinusoidal excitations.

3.1. Test-bench and samples manufacturing

We carried out tests by laying single-layer DE membranes on a flat metallic plate (serving as a low-resistance ground electrode), and casting a carbon-loaded silicone electrode layer on one face of the sample (figure 5). The dielectric membrane were made of a commercial silicone elastomer (Elastosil 2030 by Wacker) with thickness of 50 μm and relative permittivity of 2.8, largely used in DE applications [17, 54, 57]. The resulting samples emulate one half of a symmetrical DE sample (mirrored in the thickness direction) with a couple of resistive electrodes (as discussed in sections 2.2 and 2.3).

Electrode samples manufacturing was accomplished using a procedure similar to that detailed in [17] and [20], using a mixture of CB powder (Cabot Vulcan XC72) and liquid two-part silicone (Dragonskin 30 by Smooth-on). The mixture was prepared following a two-step procedure: 1 g of CB powder was first dispersed into 8 g of a volatile solvent (isopropilic alcohol) in a centrifugal planetary mixer (Thinky ARE-250). The resulting suspension was then mixed with 10 g of silicone (5 g part A + 5 g part B) and 5 g of solvent, in the same planetary mixer. The mixture was blade-cast on the DE layer using a laser-cut PET mask with thickness of 280 μm (figure 6). A PMMA structure holding a set of copper strips was subsequently applied onto the mask (see figure 5). The holder had a set of apertures to allow solvent evaporation and facilitate the cross-linking of the electrode mixture. Copper strips were attached to the bottom surface of the holder using double-sided tape of sufficient thickness ($\sim$50 μm) to ensure that the copper partially penetrates the liquid electrode when the holder is laid onto the mask. The mixture was left to cross-link at ambient temperature.

We produced samples with rectangular (strip) and circular shape (figure 7), to validate the analytical models presented in figure 3 and discussed in section 2.1. The manufactured strip sample had a length $L = 142$ mm and width $w = 18$ mm, and it held 5 equally-spaced copper strips (approximately
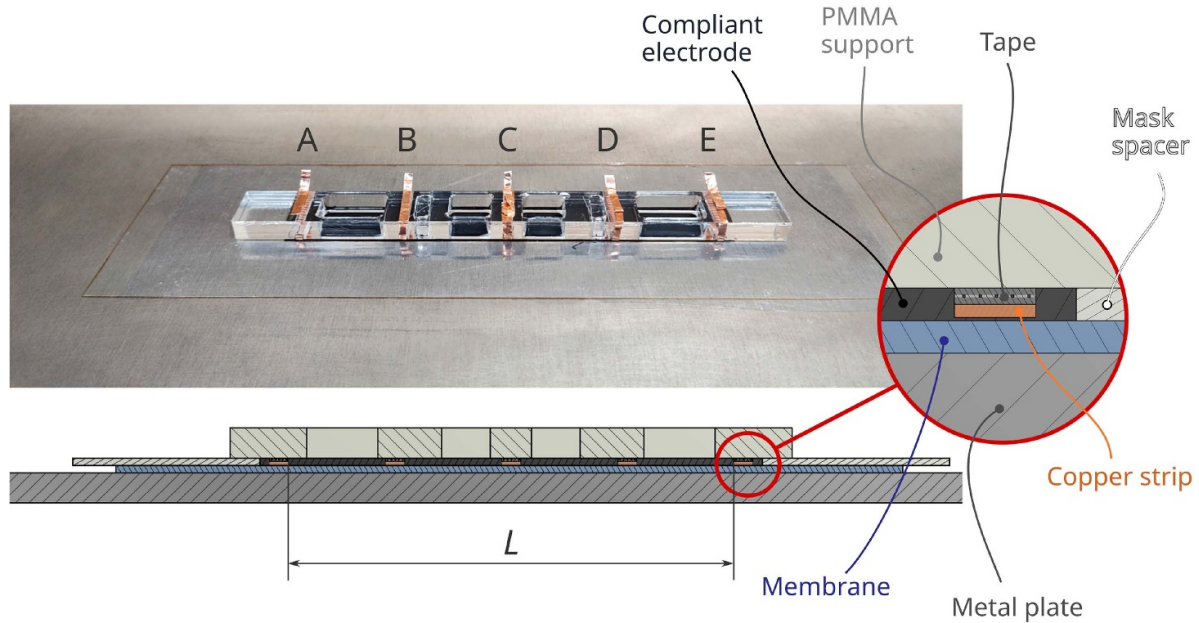
Figure 5. Photograph and schematic of the measurement setup for a rectangular strip DE sample. To reject measurement errors due to contact resistance, copper contacts were embedded into the compliant electrode bulk.

3 mm wide). During the tests, a voltage difference was applied between the ground metal plate and one of the copper connections on the strip edge.

In order to accurately measure spatial voltage distribution, copper connections were embedded during casting directly into the liquid electrode mixture before it cross-linked, rather than being merely placed on the solidified electrode. This method was chosen to mitigate the effects of contact resistance, which could otherwise compromise the accuracy of the voltage measurements at different locations on the polymer electrodes.

The circular sample had radius $R = 118$ mm, it held a continuous copper track over the circumference (where voltage was applied), and 3 equally spaced copper patches (roughly 3 mm $\times$ 3 mm) along opposite radii (at a distance of $R/4$, $2R/4$ and $3R/4$ from the centre) where voltage was measured.

We measured the resistance R_{AE} between the edge terminals of the strip sample (A and E in figure 5), and obtained an estimate of the silicone electrodes' sheet resistance as $R_s = R_m w/L$. The measured sheet resistance for the fabricated electrodes is $R_s = 6.1$ k$\Omega\square^{-1}$.

We performed measurements using sinusoidal voltage excitation at different frequencies, which allowed us to select suitable frequency ranges (for each sample) where we could observe a steady-state non-uniform voltage distribution over the electrode samples. We used frequencies between 5 and 100 kHz for the strip sample (corresponding to dimensionless angular frequencies ω^* in the range 1.9–38), and frequencies in the range 50–500 kHz for the circular sample, corresponding to ω^* in the range 3.3–33. We used an oscilloscope Siglent SDS2354X HD to both provide the excitation and acquire measurements of the voltage time-series at the different measurement points. Measurements were taken at a sample rate of 10 MS s^{-1}.

3.2. Results

We conducted tests on the two samples described in section 3.1. One has rectangular geometry and the other has circular geometry (as shown in figure 7). We subjected them to sinusoidal excitation at various frequencies. The objective was to measure the non-uniform voltage distribution generated across the surface of the DE when subjected to harmonic excitation with sufficiently high frequency.

In all tests, a voltage amplitude V_0 between 2 and 2.5 V was selected (consistently with the current limits of the instrument output ports). Although these voltages are significantly lower than the expected working voltage of DE samples with the same features as those considered here, they still allow visualising and validating the RC dynamics of interest for this work. The results for the steady-state time histories of the voltage measured at different locations on the two samples, at different frequencies, are shown in figure 8. In the figure, the dashed line represents the excitation voltage applied (and measured) at the excitation points whereas continuous lines represent experimental measurements at different points. Model predictions are represented by shaded colour bands, and they are obtained by assuming a margin of uncertainty on the value of the sheet resistance R_s (and, hence, on the value of diffusivity α introduced in equation (9) which is then used as α' in equations (13) and (16)) and the position of points where voltage is measured (which have a margin of uncertainty because the connection points embedded into the electrodes have finite size, hence locally affecting the voltage distributions). In particular, we assumed that both R_s and the positions of the measurement points are known with an uncertainty of $\pm 10\%$, we ran the model for several combinations of parameter values, and we obtained the shaded areas as the envelopes of the resulting curves. We used different excitation frequencies for the
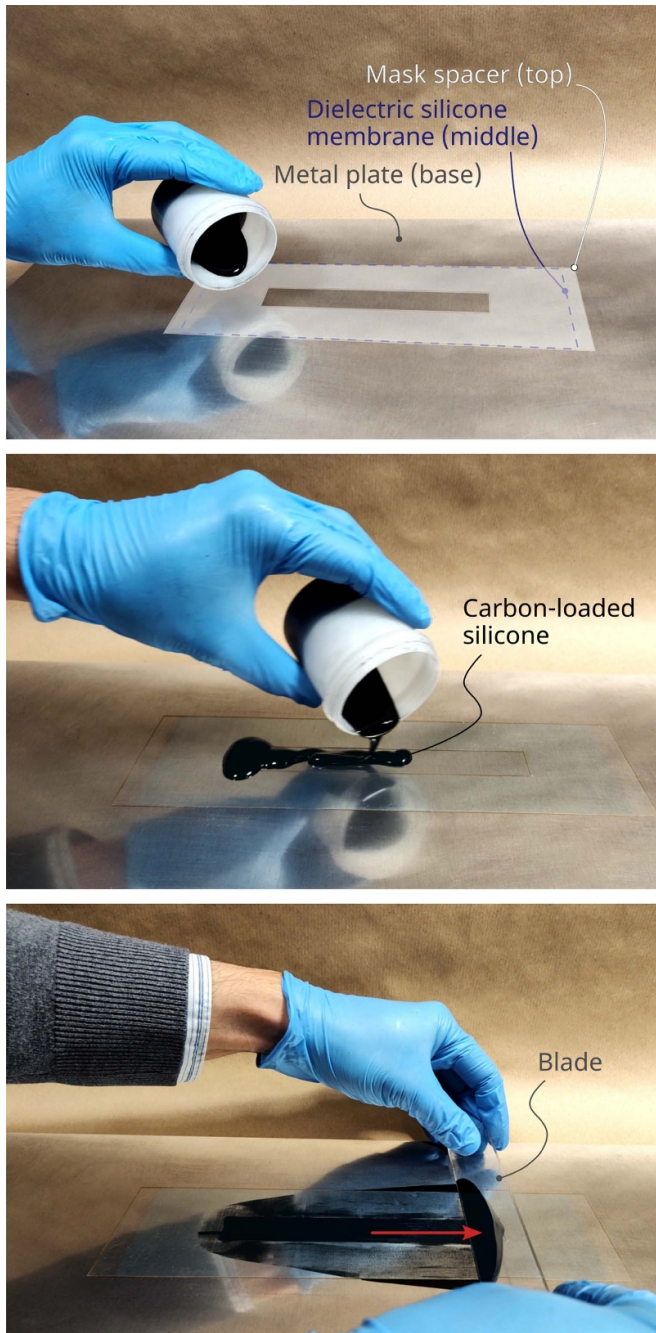
Figure 6. Steps of the manufacturing process of the compliant electrode (rectangular sample).

Figure 7. Layout of the excitation and measurement surfaces for the geometries under investigation. Brown surfaces represent the portions of electrodes where copper contacts have been embedded.

different samples, with the aim of highlighting comparable sets of dynamic responses (which are triggered by different frequencies for the two geometries under investigation). In particular, we used higher maximum frequencies for the circular capacitor sample that, as observed in section 2.3, features lower charging time than the rectangular capacitor (provided that all parameters are comparable).

The model captures the measured response with very good accuracy, as the experimental data fall within the uncertainty bands of the model practically everywhere. The dynamics follow the tr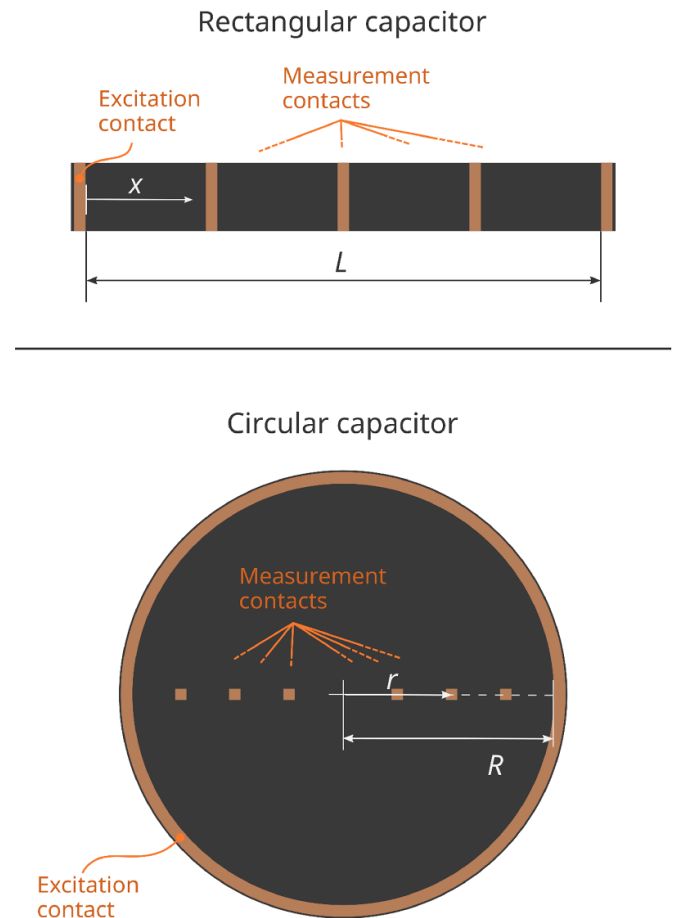ends already discussed in section 2, i.e. the voltage has a sinusoidal trend at all measurement points (confirming linearity of the dynamics), with amplitude that progressively decreases with increasing distance from the excitation points. Uncertainty in the model predictions (namely, the amplitude of the model bands) decreases for points that are further apart from the excitation surface, whereas estimates for the points in a closer proximity of prescribed voltage surfaces are more sensitive to uncertainties. This primarily happens because the phase and amplitude of the voltage waveforms far away from the excitation surfaces loosely depend on the position (x or r), rendering uncertainties on the position of the sensing points less relevant.

Figure 9 (top row) shows a set of profiles of the voltage spatial distribution at different time instants, generated using the model (with nominal parameter values), for the two geometries at selected frequencies. The envelope of such profiles is compared with the excitation amplitude measured experimentally at the different measurement points, showing again a good agreement between our diffusion model and experiments. Figure 9 (bottom row) compares the amplitudes (model vs measurements) of the voltage signals at different frequencies and different locations throughout the two samples. Results confirm that the model (fed with nominal parameters)
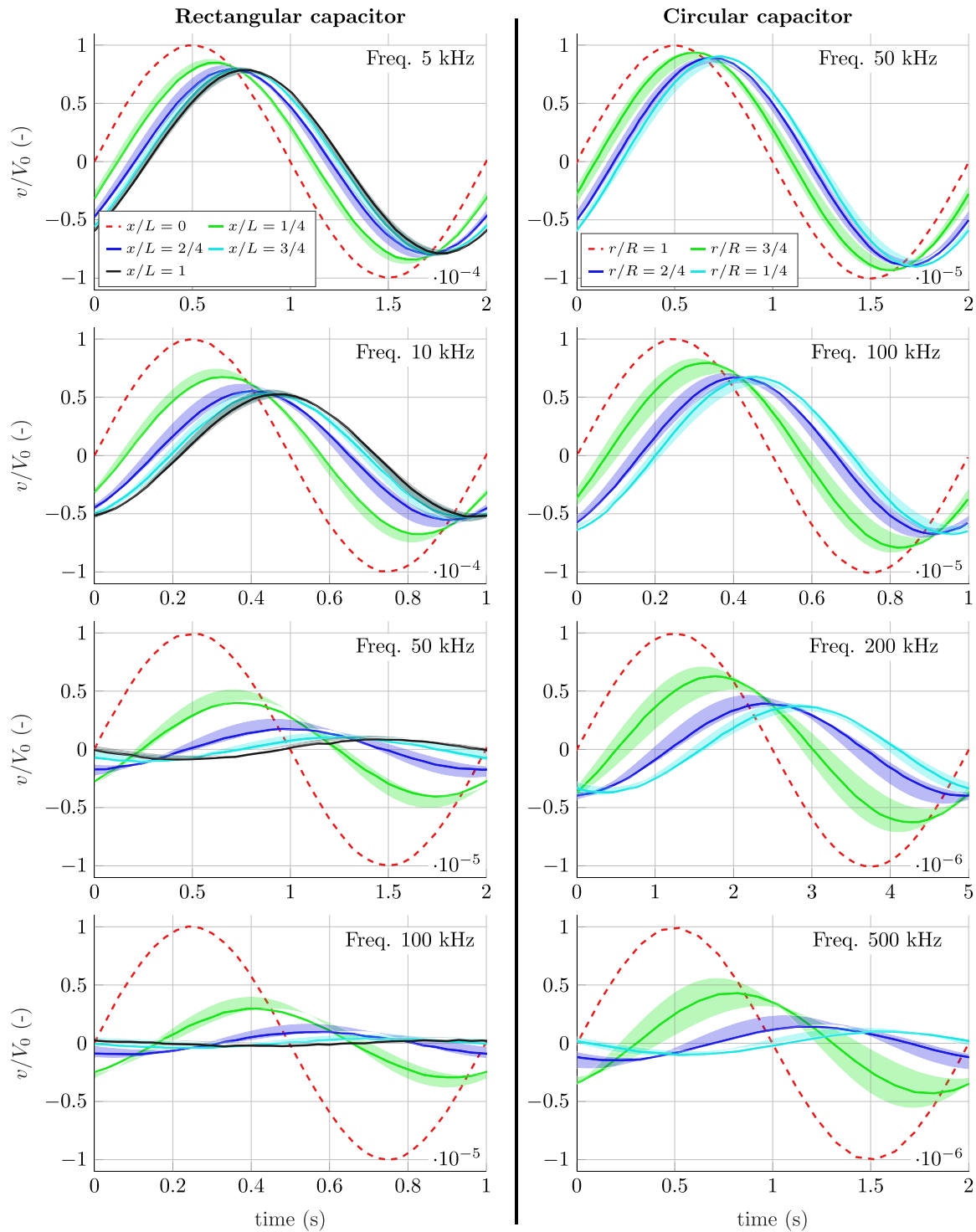
Figure 8. Comparison of experimental (solid lines) and analytical (transparent areas) voltage time histories for the rectangular (left column) and the circular (right column) capacitor samples at different input voltage (red-dashed line) frequencies. Analytical model areas are computed with 10% relative uncertainty on α and the measuring position.

effectively captures the trends in the voltage amplitude over the considered frequency range.

In conclusion, experimental data largely confirm the validity of the presented continuous diffusion model for the RC behaviour in capacitors with resistive electrodes. For the considered DE samples with silicone-based electrodes, the model

captures both the distribution of the amplitude and the phases of the voltage waveforms recorded at different locations, considering two different prototypical DE transducer geometries (rectangular and circular) and making use of a same nominal value of the sheet resistance for both samples, with no need for calibrations.
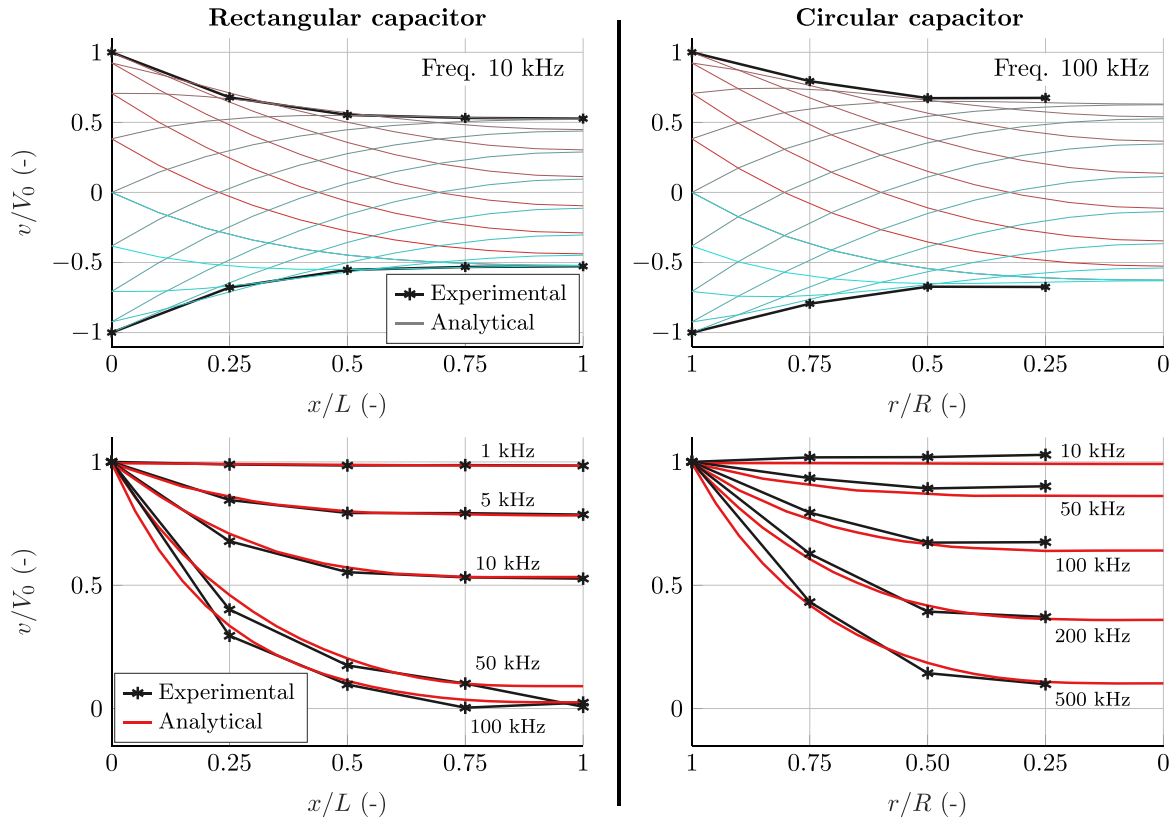
Figure 9. Comparison of experimental and analytical voltage profile amplitudes across the capacitor in steady state. On the top graphs, two specific frequencies are shown and the colour code of the analytical curves indicates the time: cyan is the start and red is the end of a period of excitation. On the bottom graphs, the analytical envelope of the peaks is compared to the experimental curves for all the tested frequencies.

4. Discussion

The analysis presented in this paper can be used to: 1) design the layout of the connections between electrodes and driving circuit (e.g. size/width of the portions of the transducer's perimeter where voltage is applied) so as to guarantee charging times/working frequencies/voltage gradients consistent with the application [46]; 2) identify functional limits (e.g. maximum working frequency) of practical EAP transducers [43]. Whereas the first point can be tackled by solving PDE problem (8) for a given connection layout and analysing the resulting voltage distributions, point 2) can be tackled by resorting to the dimensionless analysis introduced in section 2. We make reference to a generic DE transducer topology, with resistive electrodes on both DE faces, assuming same dielectric thickness and permittivity as in our experimental analyses (namely, $t_d = 50\,\mu$m and relative permittivity of 2.8, resulting in a specific capacitance of $0.5\,\mu\mathrm{F\,m}^{-2}$). We note that different transducer topologies (e.g. strip and circular capacitor examined in section 2 and, by extension, other more complex geometries) feature dimensionless charging times on the same order of magnitude. We thus take the circular capacitor topology studied in section 2.3 as reference, from which we estimated a dimensionless charging time of 0.8 (needed to bring the average voltage on the whole transducer to 99% the target

value), and a maximum dimensionless working angular frequency (here, defined as the frequency for which the voltage amplitude at the device centre is at least 90% the target value) of 2.8. Using (12), we calculate the (dimensional) charging time and limit frequency as a function of the device size (i.e. radius), assuming a sheet resistance in the range $R_s = 1 - 150\,\mathrm{k\Omega\,\square}^{-1}$. Results in figure 10(a) show that the charging time quickly grows with the device size (with a quadratic dependence). Large scale devices (e.g. metre-scale generators envisaged for wave energy harvesting applications [6]) might require charging times up to 10^0 s, if their electrodes sheet resistance is on the order of $10^5\,\mathrm{k\Omega\,\square}^{-1}$. On the other hand, implementation of thicker electrodes (with low sheet resistance) is more practical at large scales, and it would allow limiting the charging times. Centimetre-scale actuators, for which many applications have been envisaged, require charging times typically well-below milliseconds, even assuming conservative sheet resistance values. The maximum frequency at which transducers maintain nearly-constant potential over their entire surface ranges from over 10^4 Hz (with sheet resistance on the order of $10^0\,\mathrm{k\Omega\,\square}^{-1}$) to 10^3 Hz for centimetre-scale devices, making the exact value of the electrodes sheet resistance a crucial factor for loudspeakers [13, 47], or for self-sensing applications, which rely on the injection of high-frequency signals on a transducer [38, 43].
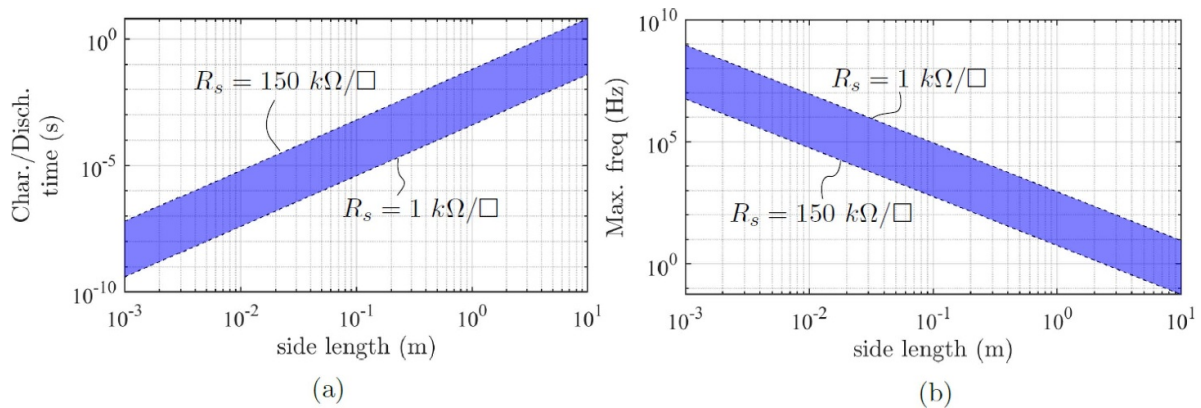
Figure 10. (a) Charging time, i.e. time to required to obtain an average voltage equal to 99% the applied voltage, over a circular device; (b) maximum working frequency i.e. frequency that provides less than 90% of the commanded sinusoidal voltage at the centre of the circular device. The data refers to a prototypical DE transducer (with $t_d = 50\,\mu$m and $\varepsilon = 2.8 \times 8.85 \cdot 10^{-12}\,\mathrm{F\,m^{-1}}$) and are reported as a function of the characteristic side length, for a range of values of the sheet resistance R_s.

Above-metre scale devices, on the other hand, might be prone to non-negligible spatial voltage gradients already with driving frequency on the order of 10^0 Hz (though their envisaged applications at scale involve frequencies on the order of 10^{-1} Hz). At such timescales, leakage current losses due to the dielectric medium resistivity (not accounted for here) might become comparable to (or more significant than) electrode losses.

The assumptions used to obtain these results are expected to hold for a broad variety of DE and EAP transducers (whose dielectric thickness and permittivity vary in a restricted range), and for multi-layer stacks (as the same considerations hold layer-wise). The considered sheet resistance values are representative of carbon-loaded elastomeric electrodes, according to values reported in literature [11, 24, 58]. The results in figure 10 thus provide reasonable and general orders of magnitude for the characteristic times/frequencies of DE transducers for realistic applications.

5. Conclusions

We investigated the electrical dynamics in electrostatic transducers with mildly resistive electrodes, with the aim of providing guidelines for electrode design and limit working ranges in EAP devices, such as DE transducers.

EAP transducers rely on compliant electrodes (e.g. carbon-loaded electrodes with relatively high sheet resistance on the order of $10^{-1} - 10^5\,\mathrm{k\Omega\square^{-1}}$), which must be able to withstand deformations while remaining conductive. As voltage is supplied through a portion of the electrodes perimeter, the electrode-dielectric assembly behaves as an RC interconnect, possibly leading to a non-homogeneous electric field distribution over the transducer surface, especially in the case of high-frequency applications. Such non-homogeneity in the voltage distribution causes part of the dielectric material to be subject to lower electric fields than requested and, hence, not to be exploited fully.

Whereas RC dynamics in EAPs are usually described using lumped RC circuits (e.g. series resistor-capacitor sets, or transmission lines with a finite number of elements), here we resorted to a continuum model, cast as a system of PDEs. Making reference to some simple prototypical geometries, we calculated semi-analytical solutions (written as Fourier series expansions) and expressed them in a dimensionless form, with the aim of extrapolating general indications regarding the charging time (i.e. the time in which a uniform potential is established over the transducer surface), and the maximum working frequency (i.e. the maximum frequency at which space gradients in the voltage amplitude are negligible) of devices.

We validated continuum models by performing measurements on silicone-based DE samples with blade-cast electrodes made of a mixture of silicone and CB. We built a setup to embed electric contacts directly into the electrodes bulk during the manufacturing process, to mitigate the effect of contact resistance. We were thus able to measure the voltage at different locations over the samples surface, in the presence of high frequency excitation. We found that the measured voltage gradients are predicted by the model with good accuracy.

Eventually, we presented a discussion on the expected orders of magnitude for charging time and maximum working frequency for DE transducers, assuming typical realistic values for the dielectric layer thickness and permittivity. We showed that changing the device scale and the electrodes sheet resistance can change the working ranges by orders of magnitude, making electrodes design a crucial aspect at high working frequencies (e.g. acoustic application) or large scales (e.g. grid-scale energy harvesting).

Data availability statement

The data cannot be made publicly available upon publication because they are not available in a format that is sufficiently

accessible or reusable by other researchers. The data that support the findings of this study are available upon reasonable request from the authors.

Acknowledgments

Appendix. Determination of ICs for the charge diffusion problem

Referring to the circuit schematisation of the system in figure 2, capacitor elements can be replaced by short-circuits at $t = 0$, leading to a same voltage distribution on opposite electrodes' nodes. Such distribution can be found as the solution to the following stationary PDE problem:

$$\begin{cases} \frac{\partial}{\partial \xi_1}\left(\frac{1}{R_s}\frac{\partial v_0}{\partial \xi_1}\right) + \frac{\partial}{\partial \xi_2}\left(\frac{1}{R_s}\frac{\partial v_0}{\partial \xi_2}\right) = 0 \\ v_0(\boldsymbol{\xi})|_{\gamma^+ \cup \gamma^-} = \bar{V}_0^+(\boldsymbol{\xi}) + \bar{V}_0^-(\boldsymbol{\xi}) \\ (\nabla v_0(\boldsymbol{\xi}) \cdot \hat{\boldsymbol{n}})|_{\Gamma \setminus (\gamma^+ \cup \gamma^-)} = 0 \end{cases} \quad (19)$$

where

$$\begin{aligned} \bar{V}_0^+(\boldsymbol{\xi}) &= \begin{cases} V^+(0), & \boldsymbol{\xi} \in \gamma^+ \\ 0, & \boldsymbol{\xi} \in \Gamma \setminus \gamma^+ \end{cases} \\ \bar{V}_0^-(\boldsymbol{\xi}) &= \begin{cases} V^-(0), & \boldsymbol{\xi} \in \gamma^- \\ 0, & \boldsymbol{\xi} \in \Gamma \setminus \gamma^- \end{cases} \end{aligned} \quad (20)$$

which has been obtained combining the second equation of system (8) (which does not contain time derivatives) and the BCs evaluated at $t = 0$. In (19), a Dirichlet type BC is applied on the portion $\gamma^+ \cup \gamma^-$ of the electrodes frontier, whereas a Neumann BC holds everywhere else.

ORCID iDs

Davide Vignotto https://orcid.org/0000-0002-7925-4702
Ion-Dan Sîrbu https://orcid.org/0000-0001-8965-9597
Marco Fontana https://orcid.org/0000-0002-5691-8115
Giacomo Moretti https://orcid.org/0000-0003-1606-7392

References

[1] Bar-Cohen Y and Anderson I A 2019 Electroactive polymer (EAP) actuators-background review *Mech. Soft Mater.* **1** 5
[2] Hajiesmaili E and Clarke D R 2021 Dielectric elastomer actuators *J. Appl. Phys.* **129** 151102
[3] Ji X, Liu X, Cacucciolo V, Imboden M, Civet Y, El Haitami A, Cantin S, Perriard Y and Shea H 2019 An autonomous untethered fast soft robotic insect driven by low-voltage dielectric elastomer actuators *Sci. Robot.* **4** eaa z6451
[4] Cao C, Gao X and Conn A T 2019 A magnetically coupled dielectric elastomer pump for soft robotics *Adv. Mater. Technol.* **4** 1900128
[5] Rothemund P, Morelle X P, Jia K, Whitesides G M and Suo Z 2018 A transparent membrane for active noise cancelation *Adv. Funct. Mater.* **28** 1800653
[6] Moretti G, Herran M S, Forehand D, Alves M, Jeffrey H, Vertechy R and Fontana M 2020 Advances in the development of dielectric elastomer generators for wave energy conversion *Renew. Sustain. Energy Rev.* **117** 109430
[7] Rothemund P, Kellaris N, Mitchell S K, Acome E and Keplinger C 2021 Hasel artificial muscles for a new generation of lifelike robots-recent progress and future opportunities *Adv. Mater.* **33** 2003375
[8] Hartmann F, Penkner L, Danninger D, Arnold N and Kaltenbrunner M 2021 Soft tunable lenses based on zipping electroactive polymer actuators *Adv. Sci.* **8** 2003104
[9] Sîrbu I-D, Moretti G, Bortolotti G, Bolignari M, Dirè S, Fambri L, Vertechy R and Fontana M 2021 Electrostatic bellow muscle actuators and energy harvesters that stack up *Sci. Robot.* **6** eaaz5796
[10] Rosset S and Shea H R 2013 Flexible and stretchable electrodes for dielectric elastomer actuators *Appl. Phys.* A **110** 281–307
[11] McCoul D, Hu W, Gao M, Mehta V and Pei Q 2016 Recent advances in stretchable and transparent electronic materials *Adv. Electron. Mater.* **2** 1500407
[12] Pelrine R, Kornbluh R D, Eckerle J, Jeuck P, Oh S, Pei Q and Stanford S 2001 Dielectric elastomers: generator mode fundamentals and applications *SPIE's 8th Annual Int. Symp. on Smart Structures and Materials* (International Society for Optics and Photonics) pp 148–56
[13] Gareis M and Maas J 2023 Wave field synthesis using buckling dielectric elastomer transducers *Smart Mater. Struct.* **32** 125024
[14] Tang C, Du B, Jiang S, Wang Z, Liu X-J and Zhao H 2024 A review on high-frequency dielectric elastomer actuators: materials, dynamics and applications *Adv. Intell. Syst.* **6** 2300047
[15] Moretti G, Rizzello G, Fontana M and Seelecke S 2022 High-frequency voltage-driven vibrations in dielectric elastomer membranes *Mechanical Systems and Signal Processing* vol 168 (All Open Access, Green Open Access)
[16] Gratz-Kelly S, Rizzello G, Fontana M, Seelecke S and Moretti G 2022 A multi-mode, multi-frequency dielectric elastomer actuator *Advanced Functional Materials* vol 32 (All Open Access, Green Open Access, Hybrid Gold Open Access)
[17] Moretti G, Righi M, Vertechy R and Fontana M 2017 Fabrication and test of an inflated circular diaphragm dielectric elastomer generator based on pdms rubber composite *Polymers* **9** 283
[18] Willian T P, Fasolt B, Motzki P, Rizzello G and Seelecke S 2023 Effects of electrode materials and compositions on the resistance behavior of dielectric elastomer transducers *Polymers* **15** 310
[19] Fasolt B, Hodgins M, Rizzello G and Seelecke S 2017 Effect of screen printing parameters on sensor and actuator performance of dielectric elastomer (DE) membranes *Sens. Actuators* A **265** 10–19
[20] Rosset S, Araromi O A, Schlatter S and Shea H R 2016 Fabrication process of silicone-based dielectric elastomer actuators *J. Vis. Exp.* **108** e53423
[21] Baechler C, Gardin S, Abuhimd H and Kovacs G 2016 Inkjet printed multiwall carbon nanotube electrodes for dielectric elastomer actuators *Smart Mater. Struct.* **25** 055009
[22] Krüger T S, Çabuk O and Maas J 2023 Manufacturing process for multilayer dielectric elastomer transducers based on

sheet-to-sheet lamination and contactless electrode application *Actuators* vol 12 (MDPI) p 95

[23] Yi J, Babick F, Strobel C, Rosset S, Ciarella L, Borin D, Wilson K, Anderson I, Richter A and Henke E-F M 2023 Characterizations and inkjet printing of carbon black electrodes for dielectric elastomer actuators *ACS Appl. Mater. Interfaces* **15** 41992–2003

[24] Michel S, Chu B T, Grimm S, Nüesch F A, Borgschulte A and Opris D M 2012 Self-healing electrodes for dielectric elastomer actuators *J. Mater. Chem.* **22** 20736–41

[25] Graz I M, Cotton D P and Lacour S P 2009 Extended cyclic uniaxial loading of stretchable gold thin-films on elastomeric substrates *Appl. Phys. Lett.* **94** 071902

[26] Ong H-Y, Shrestha M and Lau G-K 2015 Microscopically crumpled indium-tin-oxide thin films as compliant electrodes with tunable transmittance *Appl. Phys. Lett.* **107** 132902

[27] Rosset S, Niklaus M, Dubois P and Shea H R 2009 Metal ion implantation for the fabrication of stretchable electrodes on elastomers *Adv. Funct. Mater.* **19** 470–8

[28] Corbelli G, Ghisleri C, Marelli M, Milani P and Ravagnan L 2011 Highly deformable nanostructured elastomeric electrodes with improving conductivity upon cyclical stretching *Adv. Mater.* **23** 4504

[29] Lide D R 2004 *CRC Handbook of Chemistry and Physics* vol 85 (CRC Press)

[30] Jean P, Wattez A, Ardoise G, Melis C, Van Kessel R, Fourmon A, Barrabino E, Heemskerk J and Queau J 2012 Standing wave tube electro active polymer wave energy converter *SPIE Smart Structures and Materials+ Nondestructive Evaluation and Health Monitoring, Int. Society for Optics and Photonics*

[31] Benslimane M, Gravesen P and Sommer-Larsen P 2002 Mechanical properties of dielectric elastomer actuators with smart metallic compliant electrodes *Smart Structures and Materials 2002: Electroactive Polymer Actuators and Devices (EAPAD)* vol 4695 (SPIE) pp 150–7

[32] O'Brien B, Thode J, Anderson I, Calius E, Haemmerle E and Xie S 2007 Integrated Extension Sensor Based on Resistance and Voltage Measurement for a Dielectric Elastomer *Electroactive Polymer Actuators and Devices (Eapad) 2007* vol 6524 (SPIE) pp 307–17

[33] Carpi F, Chiarelli P, Mazzoldi A and De Rossi D 2003 Electromechanical characterisation of dielectric elastomer planar actuators: comparative evaluation of different electrode materials and different counterloads *Sens. Actuators* A **107** 85–95

[34] Schlaak H F, Jungmann M, Matysek M and Lotz P 2005 Novel multilayer electrostatic solid state actuators with elastic dielectric *Smart Structures and Materials 2005: Electroactive Polymer Actuators and Devices (EAPAD)* vol 5759 (SPIE) pp 121–33

[35] Schlatter S, Rosset S and Shea H 2017 Inkjet printing of carbon black electrodes for dielectric elastomer actuators *Electroactive Polymer Actuators and Devices (EAPAD) 2017* vol 10163 (SPIE) pp 177–85

[36] Hu L, Yuan W, Brochu P, Gruner G and Pei Q 2009 Highly stretchable, conductive and transparent nanotube thin films *Appl. Phys. Lett.* **94** 161108

[37] Yuan W, Lam T, Biggs J, Hu L, Yu Z, Ha S, Xi D, Senesky M K, Grüner G and Pei Q 2007 New electrode materials for dielectric elastomer actuators *Electroactive Polymer Actuators and Devices (EAPAD) 2007* vol 6524 (SPIE) pp 200–11

[38] Rosset S, O'Brien B M, Gisby T, Xu D, Shea H R and Anderson I A 2013 Self-sensing dielectric elastomer actuators in closed-loop operation *Smart Mater. Struct.* **22** 104018

[39] Rizzello G, Hodgins M, Naso D, York A and Seelecke S 2015 Modeling of the effects of the electrical dynamics on the electromechanical response of a deap circular actuator with a mass–spring load *Smart Mater. Struct.* **24** 094003

[40] Rizzello G, Fugaro F, Naso D and Seelecke S 2018 Simultaneous self-sensing of displacement and force for soft dielectric elastomer actuators *IEEE Robot. Autom. Lett.* **3** 1230–6

[41] Rizzello G, Naso D, York A and Seelecke S 2016 A self-sensing approach for dielectric elastomer actuators based on online estimation algorithms *IEEE/ASME Trans. Mech.* **22** 728–38

[42] Kahng A B, Muddu S and Vidhani D 1999 Noise and delay uncertainty studies for coupled rc interconnects *Twelfth Annual IEEE Int. ASIC/SOC Conf. (Cat. No.99TH8454)* (IEEE) pp 3–8

[43] Xu D, Michel S, McKay T, O'Brien B, Gisby T and Anderson I 2015 Sensing frequency design for capacitance feedback of dielectric elastomers *Sens. Actuators* A **232** 195–201

[44] Xu D, Tairych A and Anderson I A 2015 Stretch not flex: programmable rubber keyboard *Smart Mater. Struct.* **25** 015012

[45] Tairych A and Anderson I A 2018 A numerical method for measuring capacitive soft sensors through one channel *Smart Mater. Struct.* **27** 035016

[46] Graf C and Maas J 2012 A model of the electrodynamic field distribution for optimized electrode design for dielectric electroactive polymer transducers *Smart Mater. Struct.* **21** 094001

[47] Garnell E, Rouby C and Doaré O 2021 Resistivity-induced coupling between voltage distribution and vibrations in dielectric elastomers *Smart Mater. Struct.* **30** 025031

[48] Berger H 1972 Contact resistance and contact resistivity *J. Electrochem. Soc.* **119** 507

[49] Reeves G and Harrison H 1982 Obtaining the specific contact resistance from transmission line model measurements *IEEE Electron. Dev. Lett.* **3** 111–3

[50] Toth L A and Goldenberg A A 2002 Control system design for a dielectric elastomer actuator: the sensory subsystem *Smart Structures and Materials 2002: Electroactive Polymer Actuators and Devices (EAPAD)* vol 4695 (SPIE) pp 323–34

[51] Székely V 2018 Distributed RC Networks *Feedback, Nonlinear and Distributed Circuits* (CRC Press) pp 18–11

[52] Kufudakis A 1971 Network with lumped RC parameters as an electro-analog model of diffusion processes I. simulation of diffusion through membranes *Czech. J. Phys.* B **21** 1163–73

[53] Jeffrey A 2003 *Applied Partial Differential Equations: an Introduction* (Academic)

[54] Rizzello G, Loew P, Agostini L, Fontana M and Seelecke S 2020 A lumped parameter model for strip-shaped dielectric elastomer membrane transducers with arbitrary aspect ratio *Smart Mater. Struct.* **29** 115030

[55] Berselli G, Vertechy R, Vassura G and Parenti-Castelli V 2011 Optimal synthesis of conically shaped dielectric elastomer linear actuators: design methodology and experimental validation *IEEE/ASME Trans. Mech.* **16** 67–79

[56] Song Z-Q, Ohyama K, Shian S, Clarke D R and Zhu S 2019 Power generation performance of dielectric elastomer generator with laterally-constrained configuration *Smart Mater. Struct.* **29** 015018

[57] Albuquerque F B and Shea H 2021 Influence of electric field, temperature, humidity, elastomer material and encapsulation on the lifetime of dielectric elastomer actuators (DEAs) under DC actuation *Smart Mater. Struct.* **30** 125022

[58] Araromi O A, Rosset S and Shea H R 2015 High-resolution, large-area fabrication of compliant electrodes via laser ablation for robust, stretchable dielectric elastomer actuators and sensors *ACS Appl. Mater. Interfaces* **7** 18046–53